Engineering 32 (2024) 106–115

Contents lists available at ScienceDirect

Engineering

journal homepage: www.elsevier.com/locate/eng

Research
Environmental Engineering—Article

High Spatial Resolution Ozone Profiles Retrieved from the First Chinese Ultraviolet–Visible Hyperspectral Satellite Instrument

Fei Zhao [a,#], Cheng Liu [a,b,c,d,e,#,*], Qihou Hu [c], Congzi Xia [f], Chengxin Zhang [a], Wenjing Su [g]

[a] Department of Precision Machinery and Precision Instrumentation, University of Science and Technology of China, Hefei 230026, China
[b] Center for Excellence in Regional Atmospheric Environment, Institute of Urban Environment, Chinese Academy of Sciences, Xiamen 361021, China
[c] Key Lab of Environmental Optics and Technology, Anhui Institute of Optics and Fine Mechanics, Chinese Academy of Sciences, Hefei 230031, China
[d] Key Laboratory of Precision Scientific Instrumentation of Anhui Higher Education Institutes, University of Science and Technology of China, Hefei 230026, China
[e] Anhui Province Key Laboratory of Polar Environment and Global Change, University of Science and Technology of China, Hefei 230026, China
[f] Greater Bay Area (GBA) Branch of Aerospace Information Research Institute, Chinese Academy of Sciences, Guangzhou 510700, China
[g] Department of Environmental Science and Engineering, University of Science and Technology of China, Hefei 230026, China

ARTICLE INFO

Article history:
Received 14 November 2022
Revised 23 December 2022
Accepted 28 February 2023
Available online 7 August 2023

Keywords:
Ozone profiles
EMI
Soft calibration
Floor noise correction
Stratospheric ozone intrusion

ABSTRACT

Understanding the vertical distribution of ozone is crucial when assessing both its horizontal and vertical transport, as well as when analyzing the physical and chemical properties of the atmosphere. One of the most effective ways to obtain high spatial resolution ozone profiles is through satellite observations. The Environmental Trace Gases Monitoring Instrument (EMI) deployed on the Gaofen-5 satellite is the first Chinese ultraviolet–visible hyperspectral spectrometer. However, retrieving ozone profiles using backscattered radiance values measured by the EMI is challenging due to unavailable measurement errors and a low signal-to-noise ratio. The algorithm developed for the Tropospheric Monitoring Instrument did not allow us to retrieve 87% of the EMI pixels. Therefore, we developed an algorithm specific to the characteristics of the EMI. The fitting residuals are smaller than 0.3% in most regions. The retrieved ozone profiles were in good agreement with ozonesonde data, with maximum mean biases of 20% at five latitude bands. By applying EMI averaging kernels to the ozonesonde profiles, the integrated stratospheric column ozone and tropospheric column ozone also showed excellent agreement with ozonesonde data. The lower layers (0–7.5 km) of the EMI ozone profiles reflected the seasonal variation in surface ozone derived from the China National Environmental Monitoring Center (CNEMC). However, the upper layers (9.7–16.7 km) of the ozone profiles show different trends, with the ozone peak occurring at an altitude of 9.7–16.7 km in March, 2019. A stratospheric intrusion event in central China from August 11 to 15, 2019, is captured using the EMI ozone profiles, potential vorticity data, and relative humidity data. The increase in the CNEMC ozone concentration showed that downward transport enhanced surface ozone pollution.

1. Introduction

Ozone is a secondary trace gas in the atmosphere that varies regularly with altitude, latitude, region, season, and time. Approximately 90% of ozone is distributed between altitudes of 10–50 km, where it absorbs shortwave ultraviolet rays from sunlight (wavelength < 306.3 nm). This protects humans, animals, and plants on Earth from ultraviolet radiation [1]. The remaining 10% of the ozone is found between 9 and 10 km, is generated by chemical reactions and is transported downward from the stratosphere. However, this fraction of ozone can cause harm to human and animal skin, mucosal systems, respiratory systems, and immune systems and negatively impact vegetation growth [2]. The exchange of air between the stratosphere and troposphere enhances regional ozone pollution in the troposphere and even at the surface. Currently, China has the most severe ozone pollution of anywhere in the world [3–5]. In recent years, many strategies to control ozone pollution and improve air quality have been implemented, including desulfurization and shutting down factories [6–8]. However, controlling ozone has proven to be challenging due to the strong

* Corresponding author.
E-mail address: chliu81@ustc.edu.cn (C. Liu).
# These authors contributed equally to this work.

https://doi.org/10.1016/j.eng.2023.02.020

nonlinear relationship between the precursors that generate ozone [9]. Observations show that surface ozone levels have increased in China since 2013, though the increasing rate of ozone concentrations has slowed since 2017 [10–12]. Severe surface ozone pollution in China is largely due to strong photochemical pollution and stratospheric intrusion [13,14]. The downward transport of ozone from higher altitudes also enhances surface ozone pollution, as noted by Wang et al. [15]. Therefore, information regarding the vertical concentration of ozone is essential for researching and controlling ozone pollution.

Stratospheric intrusion can result in the downward transport of substantial amounts of ozone into the troposphere, ultimately leading to surface ozone concentrations that exceed 160 $\mu g \cdot m^{-3}$ [16]. Stratospheric intrusion typically occurs under specific meteorological conditions such as low relative humidity (RH), low tropopause height, and the folding of the potential vorticity boundary. The impact of stratospheric intrusion on ozone pollution events has been assessed in previous studies. For instance, Akritidis et al. [17] utilized assimilation data to analyze and assess a stratospheric intrusion that occurred in Europe in January 2017. Similarly, Greenslade et al. [18] evaluated the impacts of stratospheric ozone intrusion events on tropospheric ozone using an ozonesonde. Meanwhile, the vertical transport of ozone is commonly analyzed using thermal infrared radiances obtained from satellite measurements. However, there have been few studies that analyze stratospheric intrusion using ultraviolet radiances from satellite spectrometers.

The total ozone column (TOZ) has been retrieved from backscattered ultraviolet radiance measured by space-based instruments since the 1970s [19]. More recently, the Scanning Imaging Absorption Spectrometer for Atmospheric Chartography (SCIAMACHY) aboard the Environmental Satellite has provided global TOZ and stratospheric ozone profiles at a spatial resolution of 60 km × 30 km. The ultraviolet total ozone unit (TOU) onboard the Fengyun (FY)-3 satellite is the first Chinese instrument to provide daily global information on TOZ and has a spatial resolution of 50 km × 50 km [20,21]. Additionally, daily ozone profiles have been retrieved from many space-based instruments, including the Global Ozone Monitoring Experiment (GOME), which has a spatial resolution of 320 km × 40 km [22]; the Global Ozone Monitoring Experiment 2 (GOME-2) [23]; the Ozone Mapping and Profiler Suite (OMPS) [24]; the Ozone Monitoring Instrument (OMI) [25]; the Tropospheric Monitoring Instrument (TROPOMI) [26]; the Microwave Limb Sounder (MLS) [27]; the Infrared Atmospheric Sounding Interferometer (IASI) aboard the MetOp platforms; the Cross-track Infrared Sounder (CrIS), which can retrieve ozone profiles between a spectral range of 990–1070 cm^{-1} [28]; and the Atmospheric InfraRed Sounder (AIRS) [29].

Algorithms based on the optimal estimation method (OEM) are widely applied to ozone profiles retrieved from satellite observations of backscattered radiance. The OEM searches for an optimal solution that minimizes the differences between measured and simulated radiance obtained from the forward model. In addition to the calibration of measurement data, the accuracy of the forward model is also critical for the OEM during the inversion process. Liu et al. [22] calculated radiances using the Linearized Discrete Ordinate Radiative Transfer model (LIDORT) without polarization. Subsequently, the new version of Vector LIDORT (VLIDORT) is used to simulate radiances for ozone profile retrievals [30,31]. SCIATRAN V4.1 was used by Mettig et al. [26] for radiance simulations. In recent years, many efforts to retrieve ozone profiles have been performed by combining radiance measurements from multiple instruments. Joint IASI + GOME-2 [32,33], CrIS + TROPOMI [34], and AIRS + OMI [35] ozone retrievals have been conducted based on the OEM.

The Environmental Trace Gases Monitoring Instrument (EMI), which was launched on May 9, 2018, is the first Chinese hyperspectral spectrometer onboard the GaoFen-5 satellite [36,37]. The EMI is designed to monitor global information on trace gases. SO_2 vertical column density (VCD) [38], tropospheric NO_2 VCD [39], formaldehyde [40], and total ozone column [41] have been retrieved from EMI Level 1B data. However, the vertical distribution of ozone is still unavailable.

In this study, we retrieved EMI ozone profiles from the surface to an altitude of ~ 60 km using the EMI within a spectral range of 310–340 nm. The retrieved profiles, which have a vertical resolution of 2.5–3 km were utilized to evaluate the vertical transport of ozone. First, we applied a soft calibration and floor noise correction method to EMI Level 1B data. Next, we compared 1.5 years of retrieved ozone profiles with global ozonesonde station observations. Then, we also compared the retrieved tropospheric column ozone (TCO) and stratospheric column ozone (SCO) with global sounding balloon data. Furthermore, the variation between ozone measurements taken at the surface and at different altitudes below the tropopause was analyzed. Finally, we captured a stratospheric intrusion event in 2019 using EMI profiles.

2. Materials and methods

2.1. EMI data

Gaofen-5 is a sun-synchronous orbital satellite launched on May 9, 2018 and carries three EMI payloads, the directional polarization camera (DPC), and the greenhouse gases monitoring instrument (GMI). Operating at an altitude of 706 km, Gaofen-5 measures radiance at 13:30 local time. The EMI is the first nadir-viewing ultraviolet (UV)–visible (VIS) spectrometer from China capable of monitoring trace gases globally. The EMI ultraviolet channels consist of UV1 (240–315 nm) and UV2 (306–403 nm), and the visible channels consist of VIS1 (401–550 nm) and VIS2 (545–710 nm). The EMI has a swath width of 2600 km and a field of view of 114°. In this study, the EMI UV2 channel is used to retrieve ozone profiles with a spatial resolution of 12 km × 13 km (across the track × along the track).

The EMI instrument shares similar characteristics with its predecessors, TROPOMI and OMI, in terms of observation mode, spectral resolution, and orbit. However, it has a lower signal-to-noise ratio (SNR) in comparison. Specifically, the SNR of the EMI in the ultraviolet band is less than 400, as reported by Zhao et al. [36]. However, in contrast, the SNR of TROPOMI in band 3 ranges between 400 and 4000 [42]. In terms of instrument performance, the full width at half maximum (FWHM) of the EMI changes by 0.1 with cross-track position, as illustrated in Fig. 1, whereas the corresponding change for TROPOMI is only 0.02. It is important to note that the EMI measures irradiance every six months, which may pose challenges for performing daily on-orbit calibration. Furthermore, the measurement error used to constrain the inversion is not provided by the EMI Level 1B product.

2.2. Validation data

Soundings are commonly used to obtain ozone profiles from the surface to altitudes of ~35 km, and it have been utilized to validate satellite ozone measurements. The ozonesonde data used in this study was collected from November 2018 to April 2020 and has

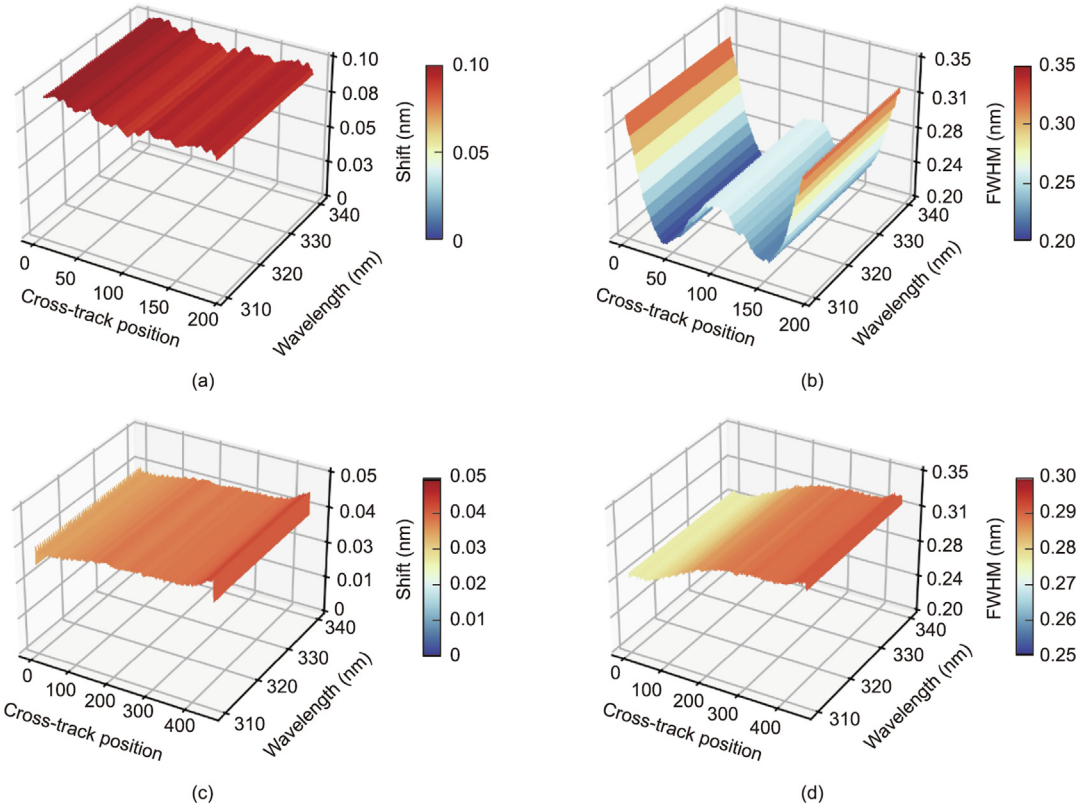

Fig. 1. (a) Shift and (b) FWHM of the EMI UV2 channel; (c) Shift and (d) FWHM of TROPOMI.

a precision of 3%–5%, an accuracy of 5%–10% [43], and a vertical resolution of 100–150 m. The ozonesonde data at low latitudes in the Southern Hemisphere were derived from the Southern Hemisphere Additional Ozonesondes (SHADOZ[†]), and the other data were obtained from the World Ozone and Ultraviolet Data Center (WOUDC[‡]). To ensure the validity of the ozonesonde data used in this study, we applied screening criteria similar to those used by Huang et al. [44]. Specifically, we selected ozonesonde data according to the following criteria: ① The correction factor is between 0.8 and 1.5, and ② bursting pressure < 200 hPa (1 hPa = 100 Pa). By applying these screening criteria, we were able to exclude anomalous data and use 98% of the dataset for validation.

The surface ozone concentration, in $\mu g \cdot m^{-3}$, was derived from the China National Environmental Monitoring Center (CNEMC) website[††]. CNEMC data have been widely used to assess exposure risk and ozone spatiotemporal characteristics [45,46]. The CNEMC measured ozone concentrations were derived using differential optical absorption spectroscopy and ultraviolet absorption spectrometry methods, with an associated measurement error of 2% and a data interval of 1 h [47]. We extracted surface ozone data for 2019 from the CNEMC website.

2.3. EMI ozone profile retrieval

In this study, we used OEM [48], which has previously been applied to TROPOMI ozone profile retrievals [49], to retrieve ozone profiles from the backscattered radiance observed by the EMI. The iterative process involved in the OEM can be described by the following equation:

$$\boldsymbol{X}_{i+1} = \boldsymbol{X}_i + \left(\boldsymbol{K}_i^{\mathrm{T}}\boldsymbol{S}_y^{-1}\boldsymbol{K}_i + \boldsymbol{S}_{\mathrm{a}}^{-1}\right)^{-1}\left\{\boldsymbol{K}_i^{\mathrm{T}}\boldsymbol{S}_y^{-1}[Y - F_i] - \boldsymbol{S}_{\mathrm{a}}^{-1}(\boldsymbol{X}_i - \boldsymbol{X}_{\mathrm{a}})\right\} \tag{1}$$

where $\boldsymbol{X}$ is the atmospheric state vector that includes the vertical ozone concentration and other auxiliary parameters. $\boldsymbol{S}_y$ is the covariance matrix of measurement uncertainty. Y represents the normalized observation. F_i is the simulated radiance generated through the forward model. We define $\Delta Y = Y - F_i$. $\boldsymbol{K}_i$ is the weighting function matrix, given by $\boldsymbol{K}_i = \partial F/\partial \boldsymbol{X}_i$. The cost function used to determine the stopping criterion for the iterative process can be summarized as:

$$\chi^2 = \left\|\boldsymbol{S}_y^{-\frac{1}{2}}[\boldsymbol{K}_i(\boldsymbol{X}_{i+1} - \boldsymbol{X}_i) - (Y - F_i)]\right\|_2^2 + \left\|\boldsymbol{S}_{\mathrm{a}}^{-\frac{1}{2}}(\boldsymbol{X}_{i+1} - \boldsymbol{X}_{\mathrm{a}})\right\|_2^2 \tag{2}$$

Here, χ^2 is the cost function.

The retrieved profile comprises 24 layers of a partial ozone column in Dobson units (DU; 1 DU = 2.69×10^{16} molecules·cm^{-2}), divided by 25 pressure levels. The initial pressure is set and then adjusted based on the tropopause pressure obtained from the US National Centers for Environmental Protection (NCEP). The state vector incorporates not only the 24 layers of the partial ozone column but also includes other variables that consider clouds, reflectivity, wavelength shifts between radiance and irradiance and between radiance and ozone cross sections, ring effect scaling, and absorption by BrO and HCHO. Further details regarding the fitting variables are listed in Table 1.

The simulated radiances were calculated using VLIDORT, a model with full linearization capability that generates analytic Jacobians with respect to the properties that characterize any atmospheric or surface parameter. The model takes into account the polarization of light that affects the modeling. In this study, we only used the single scattering rotational Raman scattering model to model the ring effect while ignoring other inelastic

[†] https://tropo.gsfc.nasa.gov/shadoz/.
[‡] https://www.woudc.org.
[††] https://www.cnemc.cn/en/.

Table 1
Details of the fitting variables and corresponding source.

Variable	Number of variables	*A priori*	*A priori* error
Ozone partial column	24	Climatology	Climatology
Cloud fraction	1	Derived from 347 nm	0.05
Surface albedo in UV2	1	Climatology	0.05
Ring scaling parameters	1	1.9	1.0
Radiance/irradiance wavelength shifts	1	0	0.02 nm
Wavelength-dependent term for reflectivity	2	0	0.01
Wavelength shifts	1	0	0.02 nm
BrO VCD	1	Climatology	1.0
HCHO VCD	1	Climatology	0.5

scattering. The radiance simulation only considers Rayleigh scattering in the atmosphere, and scattering by water vapor and aerosols is not included in this study [50]. The cloud pressure we used is derived from the TROPOMI Level 2 product [51]. In this study, the surface and clouds are assumed to be Lambertian models, and effective cloud fractions are derived at 347 nm. Additional details about VLIDORT can be found in the research of Sioris and Evans [52]. We compared the fitting residuals using MLS data, a tropopause-based (TB) climatology derived from the global ozonesonde [53], and the total ozone-dependent dynamic ozone climatology obtained from Bremen [54]. The fitting residuals from the TB climatology are smaller than those from the other two datasets (Fig. S1 in Appendix A).

Figs. 2(a)–(c) show averaging kernels (AKs) at low latitudes, midlatitudes, and high latitudes under clear sky conditions. The peak altitudes of the AKs occur below 10 hPa for all cases because observations below 310 nm are not used in this study. For the low-latitude case, the peaks above 30 km are broad and occur between 10–50 hPa. Peaks below 30 km are observed at approximately 90 hPa with subpeaks at approximately 150 hPa. The AKs at high latitudes exhibit similar characteristics to those at midlatitudes, and the peaks above 20 km occur near 20 hPa. The AK peaks below 20 km occur at 100 and 200 hPa for midlatitudes and high latitudes, respectively. The AK peaks near the surface are dislocated upward due to the large SZA and low SNR of the EMI. Figs. 2(d)–(f) show noise errors and solution errors, which are the same as in Liu et al. [25], and correspond to Figs. 2(a)–(c). The noise errors of the three cases are within 8.5%. However, the largest error at low latitudes is observed within the bottom layer, and the largest error at midlatitudes and high latitudes occurs near the tropopause. For all cases, the solution errors first decrease and then increase from the top layer to the tropopause with a minimum value of approximately 20 hPa. Below the tropopause, the solution errors show variation characteristics similar to the noise errors. The lower degree of freedom for signals (DFS) (Fig. S2 in Appendix A) in the troposphere is because measurements below 310 nm are not used, and the DFS can be improved by combining the ultraviolet and infrared observations in the future [34].

2.4. Radiometric calibration

The quality of the radiance and calibration accuracy are critical for ozone profile retrieval [26]. However, the TROPOMI algorithm experienced multiple EMI pixel retrieval failures due to the issues mentioned in Section 2.1 (Fig. S3 in Appendix A). Hence, we optimized the TROPOMI retrieval algorithm for ozone retrieved by the EMI by implementing methods such as soft calibration and correcting floor noise. To correct systematic biases in EMI Level 1B data caused by insufficient calibration and low SNR, we implemented soft calibration to improve the retrieval results. The ratio of the measured radiances to the simulated radiances and the corresponding standard deviation on April 6, 2019, are shown in Fig. 3. The difference R_{λ_i} can be written as follows [49]:

$$R_{\lambda_i} = \frac{S_{\lambda_i}}{M_{\lambda_i}} \tag{3}$$

where i is the cross-track position and R_{λ_i} is calculated from the ratio of the simulated radiance (S_{λ_i}) to the measured radiance (M_{λ_i}) at wavelength λ_i. The spectral correction was less than 0.6 at 310 nm (Fig. 3(a)). The mean differences varied from 0.6 at ~310 nm to 1.0 at 340 nm, except for the cross-track position 191, which ranged from ~0.2 to ~ 0.4. Consequently, the retrieval band window of the ozone profile is set to 310–340 nm and excludes the data at cross-track position 191. As shown in Fig. S4 in Appendix A, the soft correction spectra on different days demonstrated good consistency. Soft calibration significantly improved the retrieved results, successfully retrieving many pixels that could not be retrieved without applying the spectral correction to the EMI radiances (Fig. S3(d)).

2.5. Floor noise correction

Measurement error, which will significantly affect the sensitivity and stability of the retrieval [24], was used to constrain retrievals in the preliminary TROPOMI algorithm but is not available in the EMI Level 1B product.

The root mean square (RMS) is defined as follows:

$$\mathrm{RMS} = \sqrt{\frac{1}{N}\sum_{1}^{N}\left(\frac{\Delta Y}{\boldsymbol{S}_y^{\frac{1}{2}}}\right)^2} \tag{4}$$

where N is the number of wavelengths and $\boldsymbol{S}_y$ is the same as in Eq. (1) and ΔY is the fitting residual. An RMS of 0.05–0.10 is obtained when we first preset the floor noise to 0.5 (Fig. S3(b)). The low retrieved RMS indicated after fitting prompted us to compute the floor noise correction spectrum using the standard deviations derived from the spectral fitting residuals (Fig. 4). Without applying floor noise correction, the averaging fitting residual (AFR) ranged from ~1.6% to ~0.3% between 60°S–60°N (Fig. S3(c)). The retrieved results were significantly improved after applying floor noise correction. The RMS (Fig. S3(b)) increased from ~0.8 to 1.1, and the AFR (Fig. S3(c)) decreased about 0.1%–0.3% in the Northern Hemisphere. The average TCO varies from 33.02 to 34.89 DU after applying floor noise correction (Fig. S3(a)). However, in the Southern Hemisphere, the AFR improvement is smaller due to the large SZA. Thus, floor noise error is used as a constraint in EMI ozone profile retrievals. To improve computing speed, we added four pixels along the orbital direction.

3. Results and discussion

3.1. Validation with ozonesonde

Fig. 5 shows a comparison of the results of the retrieved partial ozone column and ozonesonde observations. The ozonesonde TCO is defined as the partial column between the surface and tropopause derived from NCEP, while the integral of the ozonesonde profile from the tropopause to the bursting pressure is taken as the SCO. To eliminate the impact of different vertical resolutions, we reduce the ozonesonde profile to the same resolution as the EMI by using the EMI AK. For comparison with the EMI, *a priori* and ozonesonde TCO with 762 coincident pairs are shown in

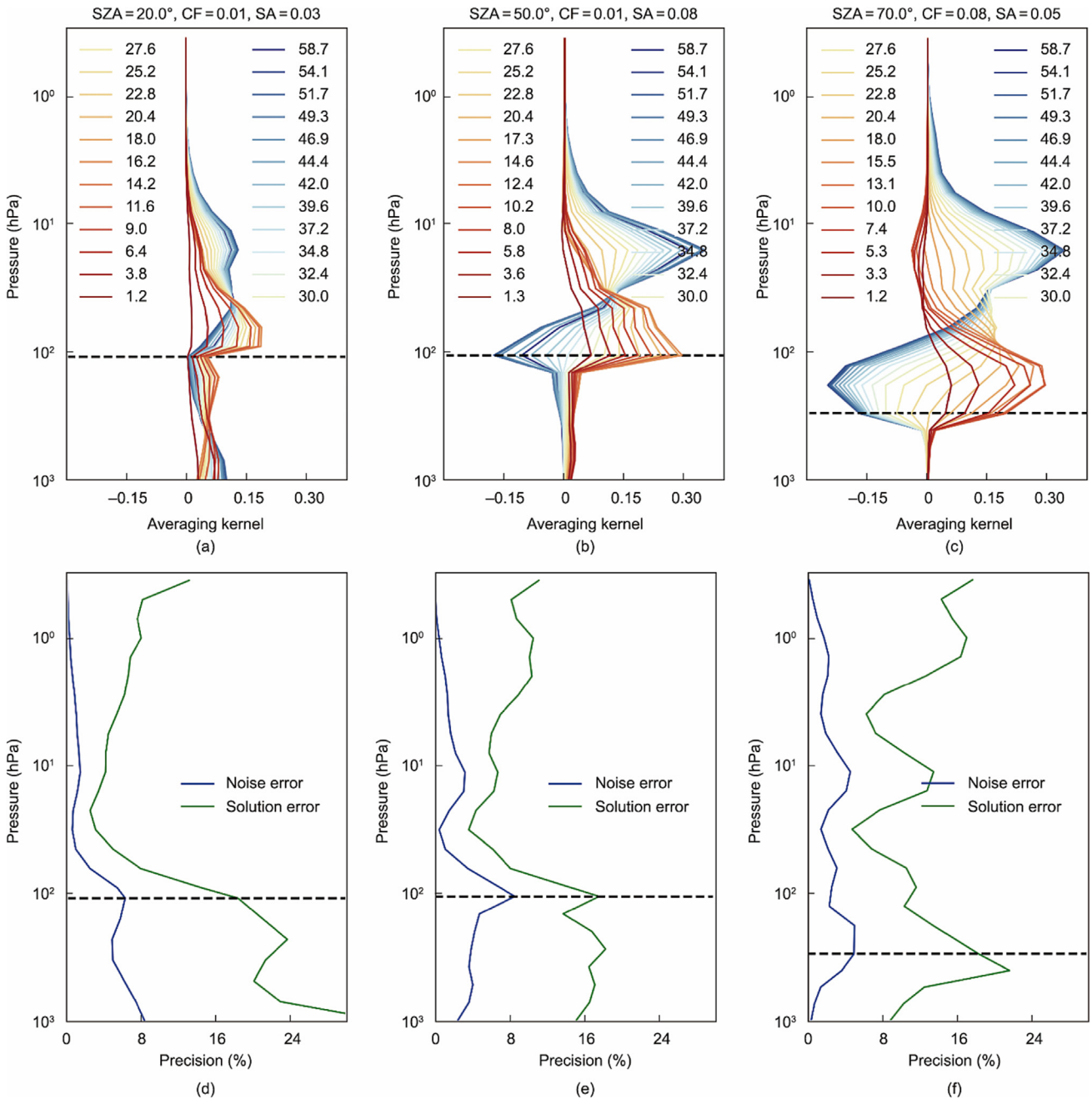

Fig. 2. (a–c) Averaging kernels for three scenarios: (a) low latitudes, (b) midlatitudes, and (c) high latitudes with a nearly clear sky. The solar zenith angle (SZA), cloud fraction (CF), and surface albedo (SA) are shown in the titles. The altitude of the averaging kernels is shown in the legend, and the black horizontal dashed line indicates the tropopause. (d–f) Noise error and solution error corresponding to (a–c).

Fig. 5(a). The mean TCO bias between the ozonesonde and *a priori* results is −2.0 DU with a standard deviation of 4.0 DU. The slope between the retrieved and ozonesonde TCO without convolving with the EMI AK is 0.645, and the mean bias is 0.5 DU with a standard deviation of 7.8 DU. After applying the retrieved AK to the ozonesonde profile, the correlation coefficient increased from 0.714 to 0.906, and the mean bias increased to 1.1 DU with a standard deviation of 4.1 DU and slope of 1.027. The prior SCO showed a large bias of −7.0 DU when compared with the ozonesonde SCO (Fig. 5(b)). The retrieval remarkably improved the standard deviation over the *a priori* standard deviation. The mean bias and correlation coefficient obtained with the EMI AK were 7.5 DU and 0.955, respectively. Applying the EMI AK to the ozonesonde profile, the slope ranged from 0.947 to 0.954.

A comparison of the retrieved ozone profiles and ozonesonde results for five latitude bands is shown in Fig. S6 in Appendix A. The retrieved ozone profiles showed good agreement with the ozonesonde profiles at all bands. Latitudinally, consistency was better at low latitudes than at high latitudes, but the larger mean bias in the tropics may be due to "drop off." The mean biases were large between 10–100 hPa but remained within 10% above 10 hPa for all latitude bands. The standard deviation between 10–100 hPa was significantly reduced in the tropics and midlatitudes. However, in the bottom seven layers, the standard deviation was larger than that in the *a priori* comparison at high latitudes, which may be due to the lower SNR and soft calibration spectrum calculated from the tropics, thereby weakening the correction effect for high latitudes.

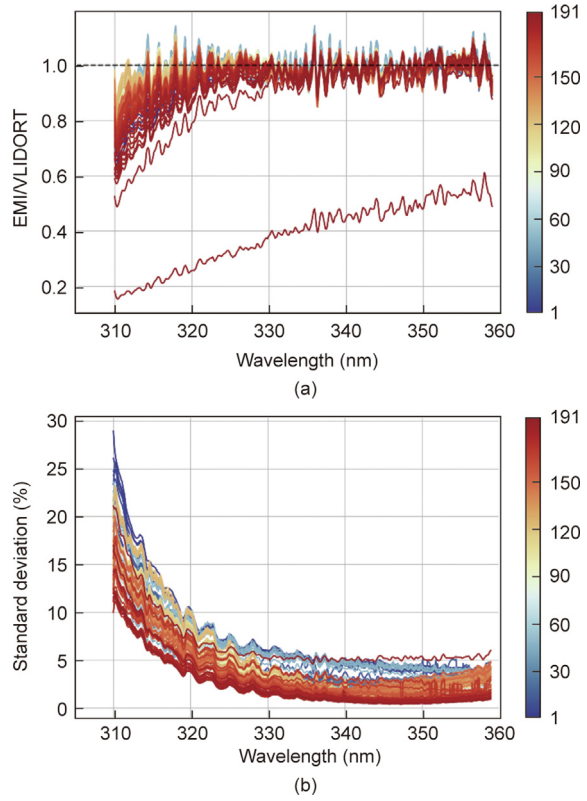

Fig. 3. (a) Soft calibration spectrum calculated from measured radiance (EMI) and simulated radiances (VLIDORT) on April 6, 2019. (b) The corresponding standard deviation of the soft calibration spectrum. The 191 cross-track positions are indicated in different colors. The radiances from 340 to 360 nm are not used in our retrievals due to the weak absorption of ozone.

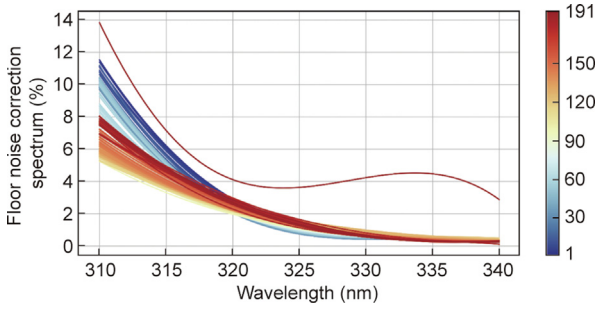

Fig. 4. The calculated floor noise correction spectrum on April 6, 2019. The 191 cross-track positions are shown in different colors.

3.2. Annual variation in ozone at different layers in China

Several studies have investigated the variable trends and characteristics of surface ozone. Fig. 6 shows seasonal variations over the Beijing–Tianjin–Hebei (BTH) region. The monthly mean surface ozone was calculated from the daily CNEMC ozone concentration between 13:00 and 14:00 China Standard Time (CST). The monthly mean values of ozone concentration over the BTH region displayed single-peak patterns. The monthly mean ozone in China steadily increased from January to June, peaked at 168 $\mu g \cdot m^{-3}$ in June 2019, and then decreased from September onwards. The bottom three layers of the retrieved EMI ozone profiles showed good agreement with the CNEMC data and demonstrated a good ability to capture the monthly trends of surface ozone. However, the upper three layers of ozone, with altitudes between 9.7 and

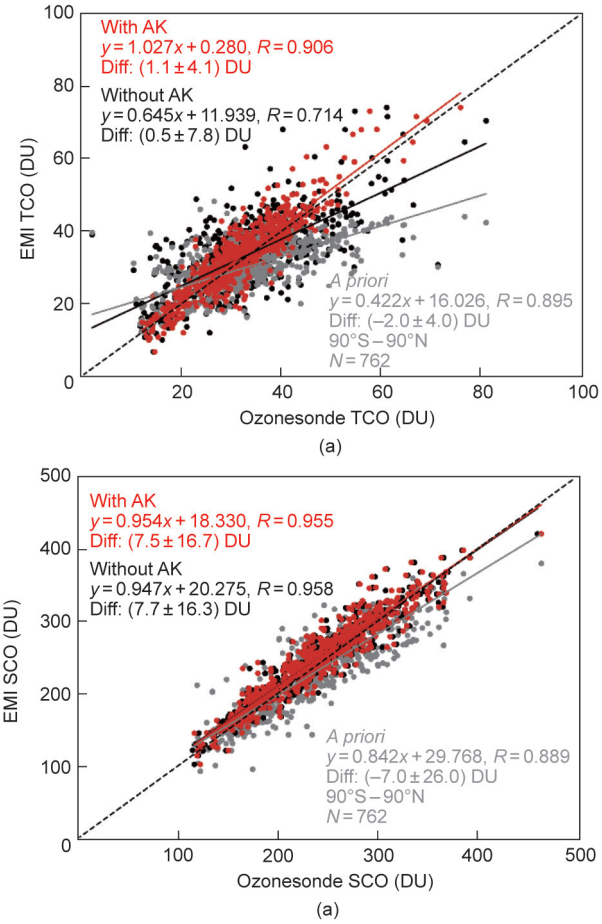

Fig. 5. (a) Scatter plots of EMI and ozonesonde TCO with (red) and without (black) EMI averaging kernels. Scatter plots of *a priori* vs ozonesonde results are shown in gray. (b) Similar to (a) but for SCO from November 2018 to April 2020.

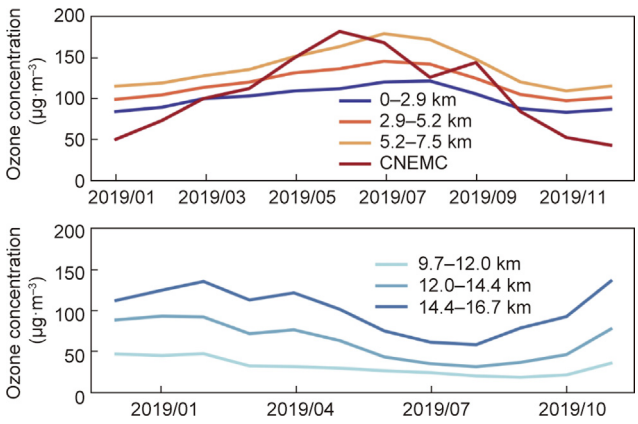

Fig. 6. Time series of monthly mean CNEMC data and retrieved ozone profiles over the Beijing–Tianjin–Hebei region at different altitudes from January to December 2019. Ozone concentrations at different altitudes are shown in different colors.

16.7 km, showed different trends compared to surface ozone. The upper three ozone layers decreased after March and increased after September, with low ozone concentrations occurring between September and October. Previous research has reported that stratospheric intrusion, which brings substantial amounts of ozone into the troposphere, frequently occurs during spring and winter in the mid-northern latitudes [55,56]. The high concentration of the retrieved profile between 9.7 and 16.7 km was observed during

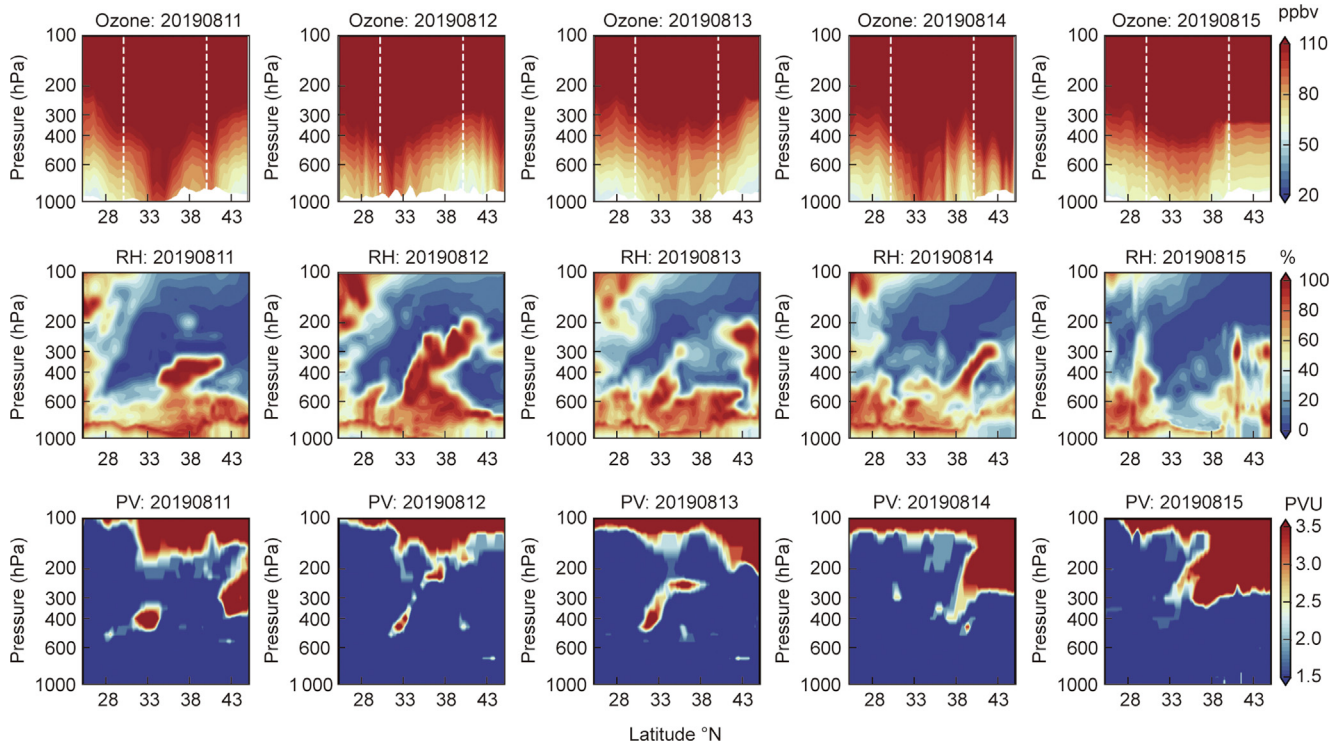

Fig. 7. Variations in ozone profiles, RH, and PV between 25°N and 45°N at 115°E from August 11 to 15, 2019. ppbv: part per billion by volume.

winter and spring. Thus, it is possible to use EMI profiles to analyze the vertical transport of ozone near the surface.

3.3. A case of stratospheric ozone intrusion in China

Potential vorticity (PV) is a widely used tracer to identify stratospheric ozone intrusion [17,57]. Ozone and PV exhibit wide variations from the troposphere to the stratosphere, and the intrusion of stratospheric air into the troposphere results in the vertical transport of large amounts of ozone and dry air with high PV values. In this study, we use the relative humidity and PV profiles obtained from the European Centre for Medium-Range Weather Forecasts (ECMWF). The 2 PVU (1 PVU = 10^{-6} K · kg^{-1} · m^2 · s^{-1}) isobaric surface is commonly used as the dynamic tropopause [17,18]. Previous studies have demonstrated a negative correlation between ozone and carbon monoxide during stratospheric intrusion [57,58].

We identified a stratospheric intrusion event in central China from August 11 to 15, 2019, using the EMI ozone profiles, PV, and humidity data from ECMWF. Fig. 7 shows the latitudinal cross sections of ozone, RH and PV at 115°E from August 11 to 15, 2019. High ozone values occur between 30°N and 35°N, which were caused by the stratospheric folding event. The area where PV is greater than 2 PVU sinks below 500 hPa on August 11 to 13 and below 400 hPa on August 14 and 15, with a corresponding RH of less than 20%.

We also assessed the impact of the intrusion event on surface ozone concentrations by analyzing carbon monoxide and ozone data from CNEMC. Kaifeng (34.7967°N, 114.2886°E) (Fig. 8), Luohe (32.965°N, 114.018°E) (Fig. S7 in Appendix A), and Xinyang (32.1078°N, 114.1044°E) (Fig. S8 in Appendix A) in Henan Province are analyzed below. The maximum daily 8 h average (MDA8) ozone concentrations for each city are shown in Table 2. Between August 10 and 15, the MDA8 ozone concentrations in all three cities increased rapidly, with maximum concentrations exceeding 160 μg·m^{-3} (Secondary National Ambient Air Quality Standards) on August 15.

The EMI ozone vertical distribution, RH, PV, and CNEMC data in Kaifeng are analyzed, and the other two cities are shown in Appendix A. In Kaifeng, high ozone values below 500 hPa were observed on August 11, 13, and 15. During these periods, PV values were high, and relative humidity was less than 30%. The hourly time series of surface ozone and carbon monoxide in Kaifeng show an anti-correlation (Fig. 8(c)). Similar characteristics were observed in the other two cases. The EMI profiles indicated that ozone greater than 70 parts per billion (ppb) sank below 800 hPa from August 11 to 15, except on August 12 and 14. The PV and RH in the mid-low troposphere also demonstrated a negative correlation. The time series data from CNEMC demonstrated that the anti-correlation between the surface ozone and carbon monoxide was influenced by the stratospheric intrusion.

4. Conclusions

This research presents the first ozone profiles retrieved from the EMI and derived backscattered UV radiances using the OEM. To improve the retrievals, soft calibration and floor noise correction were applied. We obtained the corrected spectrum by comparing the simulated radiance, calculated by VLIDORT using MLS profiles as *a priori* values, and measured radiances at low latitudes. Soft calibration corrected the systematic bias of EMI Level 1B data, which resulted in successful retrievals of many previously failed pixels. To address the lack of measurement error information for the EMI Level 1B data, we preset the constraint as 0.5 and obtained the constraint by fitting the standard deviation of the inversion residuals. After soft calibration and floor noise correction, the accuracy of the fitting residuals and RMS significantly improved. However, the retrieved profiles still had a large error in the middle and high latitudes, which was limited by the low SNR of the EMI.

We compared the retrieved results with ozonesonde measurements. The EMI TCO and SCO agreed with ozonesonde measurements, with correlation coefficients of 0.906 and 0.955,

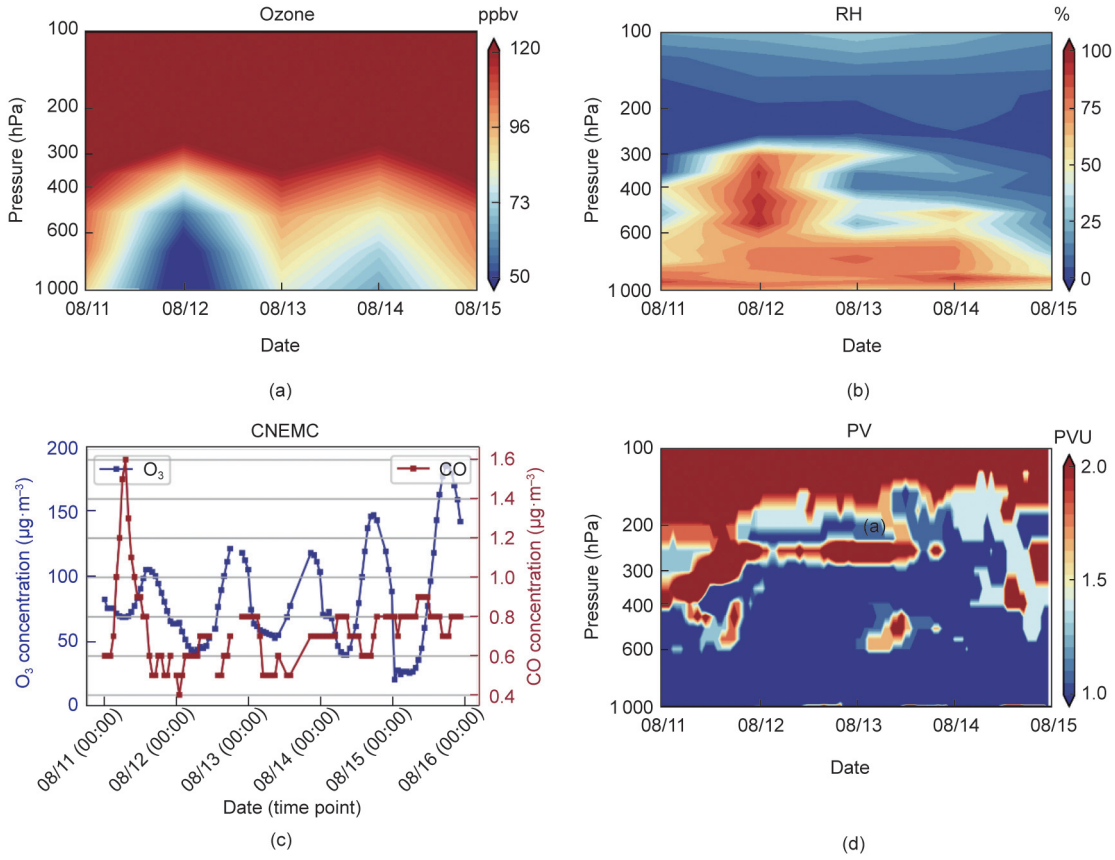

Fig. 8. Trends of the (a) ozone profile, (b) RH, (c) time series of 8 h average ozone (blue) and hourly mean carbon monoxide (red) concentrations, and (d) PV in Kaifeng between August 11 and 15, 2019.

Table 2
The MDA8 ozone concentration (μg·m^{-3}) of the three cities in 2019.

Date	Kaifeng	Luohe	Xinyang
2019-08-10	105	88	100
2019-08-11	106	127	133
2019-08-12	122	136	128
2019-08-13	119	116	143
2019-08-14	148	129	160
2019-08-15	187	180	172

respectively. The EMI TCO showed a positive bias of 1.1 DU compared to ozonesonde TCO. The mean SCO bias between the EMI and ozonesonde data was 7.5 DU with a standard deviation of 16.7 DU. Ozonesonde profiles from five latitude bands were also used to validate the EMI ozone profiles. The mean biases of the ozone profiles derived from the EMI and ozonesonde data were within 20%, and the standard deviation in UTLS decreased relative to the *a priori* values. However, a large standard deviation was observed in the bottom seven layers.

The bottom layers in the EMI ozone profiles were consistent with the measured surface ozone concentration. The upper layers in the EMI ozone profiles exhibited opposite seasonal cycles compared to the surface ozone concentrations from CNEMC. At an altitude of 9.7–16.7 km, high ozone values were noted in the EMI data during spring and winter, and low values were observed in September and October. A stratospheric intrusion event from August 11 to 15, 2019, was observed using the EMI ozone profiles combined with PV data and relative humidity data obtained from the ECMWF. Tropopause folding vertically transports a large amount of dry air and ozone into the troposphere and even the surface layers, resulting in an increase in ozone concentrations at ground level. The surface ozone concentration exhibited a negative correlation with carbon monoxide, and the MDA8 ozone concentration exceeded 160 μg·m^{-3} in all three cases. The EMI ozone profile was crucial for studying the vertical transport of ozone.

Acknowledgments

This work was supported by the National Natural Science Foundation of China (42225504 and 41977184), the Strategic Priority Research Program of the Chinese Academy of Sciences (XDA23020301), the Key Research and Development Project of Anhui Province (202104i07020002), the Major Projects of High Resolution Earth Observation Systems of National Science and Technology (05-Y30B01-9001-19/20-3), the Key Laboratory of Atmospheric Chemistry/China Meteorological Administration (LAC/CMA) (2022B06), and the Youth Innovation Promotion Association of the Chinese Academy of Sciences (2021443).

Compliance with ethics guidelines

Fei Zhao, Cheng Liu, Qihou Hu, Congzi Xia, Chengxin Zhang, and Wenjing Su declare that they have no conflict of interest or financial conflicts to disclose.

Appendix A. Supplementary data

Supplementary data to this article can be found online at https://doi.org/10.1016/j.eng.2023.02.020.

References

[1] Norval M, Cullen AP, de Gruijl FR, Longstreth J, Takizawa Y, Lucas RM, et al. The effects on human health from stratospheric ozone depletion and its interactions with climate change. Photochem Photobiol Sci 2007;6:232–51.
[2] Nuvolone D, Petri D, Voller F. The effects of ozone on human health. Environ Sci Pollut Res Int 2018;25:8074–88.
[3] Ma J, Xu X, Zhao C, Yan P. A review of atmospheric chemistry research in China: photochemical smog, haze pollution, and gas–aerosol interactions. Adv Atmos Sci 2012;29:1006–26.
[4] Che H, Xia X, Zhao H, Dubovik O, Holben BN, Goloub P, et al. Spatial distribution of aerosol microphysical and optical properties and direct radiative effect from the China Aerosol Remote Sensing Network. Atmos Chem Phys 2019;19:11843–64.
[5] Zhang C, Liu C, Hu Q, Cai Z, Su W, Xia C, et al. Satellite UV–Vis spectroscopy: implications for air quality trends and their driving forces in China during 2005–2017. Light Sci Appl 2019;8:100.
[6] Lu X, Zhang S, Xing J, Wang Y, Chen W, Ding D, et al. Progress of air pollution control in China and its challenges and opportunities in the ecological civilization era. Engineering 2020;6:1423–31.
[7] Wang S, Hao J. Air quality management in China: issues, challenges, and options. J Environ Sci 2012;24:2–13.
[8] Liu C, Xing C, Hu Q, Li Q, Liu H, Hong Q, et al. Ground-based hyperspectral stereoscopic remote sensing network: a promising strategy to learn coordinated control of O_3 and $PM_{2.5}$ over China. Engineering 2022;19:71–83.
[9] Wang T, Xue L, Brimblecombe P, Lam YF, Li L, Zhang L. Ozone pollution in China: a review of concentrations, meteorological influences, chemical precursors, and effects. Sci Total Environ 2017;575:1582–96.
[10] Wang W, Parrish DD, Wang S, Bao F, Ni R, Li X, et al. Long-term trend of ozone pollution in China during 2014–2020: distinct seasonal and spatial characteristics and ozone sensitivity. Atmos Chem Phys 2022;22:8935–49.
[11] Maji KJ, Namdeo A. Continuous increases of surface ozone and associated premature mortality growth in China during 2015–2019. Environ Pollut 2021;269:116183.
[12] Lu X, Zhang L, Wang X, Gao M, Li K, Zhang Y, et al. Rapid increases in warm-season surface ozone and resulting health impact in China since 2013. Environ Sci Technol Lett 2020;7:240–7.
[13] Qin T, Wang J, Li R, Fang C. Diurnal and inter-annual variability of surface ozone in Baicheng region. China Tellus B Chem Phys Meteorol 2021;73:1–10.
[14] Xu W, Xu X, Lin M, Lin W, Tarasick D, Tang J, et al. Long-term trends of surface ozone and its influencing factors at the Mt Waliguan GAW station, China—part 2: the roles of anthropogenic emissions and climate variability. Atmos Chem Phys 2018;18:773–98.
[15] Wang Y, Wang H, Wang W. A stratospheric intrusion-influenced ozone pollution episode associated with an intense horizontal-trough event. Atmos 2020;11:164.
[16] Wang X, Wu Y, Randel W, Tilmes S. Stratospheric contribution to the summertime high surface ozone events over the western united states. Environ Res Lett 2020;15(10):1040a6.
[17] Akritidis D, Katragkou E, Zanis P, Pytharoulis I, Melas D, Flemming J, et al. A deep stratosphere-to-troposphere ozone transport event over Europe simulated in CAMS global and regional forecast systems: analysis and evaluation. Atmos Chem Phys 2018;18:15515–34.
[18] Greenslade JW, Alexander SP, Schofield R, Fisher JA, Klekociuk AK. Stratospheric ozone intrusion events and their impacts on tropospheric ozone in the Southern Hemisphere. Atmos Chem Phys 2017;17:10269–90.
[19] Bhartia PK, McPeters RD, Mateer CL, Flynn LE, Wellemeyer C. Algorithm for the estimation of vertical ozone profiles from the backscattered ultraviolet technique. J Geophys Res D Atmospheres 1996;101:18793–806.
[20] Wang Y, Wang Y, Wang W, Zhang Z, Lü J, Fu L, et al. FY-3 satellite ultraviolet total ozone unit. Chin Sci Bull 2010;55:84–9.
[21] Zhang XX, Chen B, He F, Song KF, He LP, Liu SJ, et al. Wide-field auroral imager onboard the Fengyun satellite. Light Sci Appl 2019;8:47.
[22] Liu X, Chance K, Sioris CE, Spurr RJD, Kurosu TP, Martin RV, et al. Ozone profile and tropospheric ozone retrievals from the Global Ozone Monitoring Experiment: algorithm description and validation. J Geophys Res 2005;110(D20):D20307.
[23] Miles GM, Siddans R, Kerridge BJ, Latter BG, Richards NAD. Tropospheric ozone and ozone profiles retrieved from GOME-2 and their validation. Atmos Meas Tech 2015;8:385–98.
[24] Bak J, Liu X, Kim JH, Haffner DP, Chance K, Yang K, et al. Characterization and correction of OMPS nadir mapper measurements for ozone profile retrievals. Atmos Meas Tech 2017;10:4373–88.
[25] Liu X, Bhartia PK, Chance K, Spurr RJD, Kurosu TP. Ozone profile retrievals from the Ozone Monitoring Instrument. Atmos Chem Phys 2010;10:2521–37.
[26] Mettig N, Weber M, Rozanov A, Arosio C, Burrows JP, Veefkind P, et al. Ozone profile retrieval from nadir TROPOMI measurements in the UV range. Atmos Meas Tech 2021;14:6057–82.
[27] Barath FT, Chavez MC, Cofield RE, Flower DA, Frerking MA, Gram MB, et al. The Upper Atmosphere Research Satellite microwave limb sounder instrument. J Geophys Res D Atmospheres 1993;98:10751–62.
[28] Ma P, Chen L, Wang Z, Zhao S, Li Q, Tao M, et al. Ozone profile retrievals from the Cross-Track Infrared Sounder. IEEE Trans Geosci Remote Sens 2016;54:3985–94.
[29] Goldberg MD, Qu Y, McMillin LM, Wolf W, Lihang Z, Divakarla M. AIRS near-real-time products and algorithms in support of operational numerical weather prediction. IEEE Trans Geosci Remote Sens 2003;41:379–89.
[30] Fu D, Worden JR, Liu X, Kulawik SS, Bowman KW, Natraj V. Characterization of ozone profiles derived from Aura TES and OMI radiances. Atmos Chem Phys 2013;13:3445–62.
[31] Bak J, Liu X, Spurr R, Yang K, Nowlan CR, Miller CC, et al. Radiative transfer acceleration based on the principal component analysis and lookup table of corrections: optimization and application to UV ozone profile retrievals. Atmos Meas Tech 2021;14:2659–72.
[32] Costantino L, Cuesta J, Emili E, Coman A, Foret G, Dufour G, et al. Potential of multispectral synergism for observing ozone pollution by combining IASI-NG and UVNS measurements from the EPS-SG satellite. Atmos Meas Tech 2017;10:1281–98.
[33] Cuesta J, Eremenko M, Liu X, Dufour G, Cai Z, Höpfner M, et al. Satellite observation of lowermost tropospheric ozone by multispectral synergism of IASI thermal infrared and GOME-2 ultraviolet measurements over Europe. Atmos Chem Phys 2013;13:9675–93.
[34] Mettig N, Weber M, Rozanov A, Burrows JP, Veefkind P, Thompson AM, et al. Combined UV and IR ozone profile retrieval from TROPOMI and CrIS measurements. Atmos Meas Tech 2022;15:2955–78.
[35] Fu D, Kulawik SS, Miyazaki K, Bowman KW, Worden JR, Eldering A, et al. Retrievals of tropospheric ozone profiles from the synergism of AIRS and OMI: methodology and validation. Atmos Meas Tech 2018;11:5587–15505.
[36] Zhao MJ, Si FQ, Zhou HJ, Wang SM, Jiang Y, Liu WQ. Preflight calibration of the Chinese Environmental Trace Gases Monitoring Instrument (EMI). Atmos Meas Tech 2018;11:5403–19.
[37] Zhang C, Liu C, Wang Y, Si F, Zhou H, Zhao M, et al. Preflight evaluation of the performance of the Chinese Environmental Trace Gas Monitoring Instrument (EMI) by spectral analyses of nitrogen dioxide. IEEE Trans Geosci Remote Sens 2018;56:3323–32.
[38] Xia C, Liu C, Cai Z, Zhao F, Su W, Zhang C, et al. First sulfur dioxide observations from the Environmental Trace Gases Monitoring Instrument (EMI) onboard the GeoFen-5 satellite. Sci Bull 2021;66:969–73.
[39] Zhang C, Liu C, Chan KL, Hu Q, Liu H, Li B, et al. First observation of tropospheric nitrogen dioxide from the Environmental Trace Gases Monitoring Instrument onboard the GaoFen-5 satellite. Light Sci Appl 2020;9:66.
[40] Su W, Liu C, Hu Q, Zhang C, Liu H, Xia C, et al. First global observation of tropospheric formaldehyde from Chinese GaoFen-5 satellite: locating source of volatile organic compounds. Environ Pollut 2022;297:118691.
[41] Qian Y, Luo Y, Si F, Zhou H, Yang T, Yang D, et al. Total ozone columns from the Environmental Trace Gases Monitoring Instrument (EMI) using the DOAS method. Remote Sens 2021;13(11):2098.
[42] Kleipool Q, Ludewig A, Babić L, Bartstra R, Braak R, Dierssen W, et al. Pre-launch calibration results of the TROPOMI payload on-board the Sentinel-5 Precursor satellite. Atmos Meas Tech 2018;11(12):6439–79.
[43] Smit HGJ, Straeter W, Johnson BJ, Oltmans SJ, Davies J, Tarasick DW, et al. Assessment of the performance of ECC-ozonesondes under quasi-flight conditions in the environmental simulation chamber: insights from the Juelich Ozone Sonde Intercomparison Experiment (JOSIE). J Geophys Res D Atmospheres 2007;112(D19):D19306.
[44] Huang G, Liu X, Chance K, Yang K, Bhartia PK, Cai Z, et al. Validation of 10-year SAO OMI Ozone Profile (PROFOZ) product using ozonesonde observations. Atmos Meas Tech 2017;10:2455–75.
[45] Gao L, Yue X, Meng X, Du L, Lei Y, Tian C, et al. Comparison of ozone and $PM_{2.5}$ concentrations over urban, suburban, and background sites in China. Adv Atmos Sci 2020;37:1297–309.
[46] Sun Y, Yin H, Lu X, Notholt J, Palm M, Liu C, et al. The drivers and health risks of unexpected surface ozone enhancements over the Sichuan Basin, China, in 2020. Atmos Chem Phys 2021;21:18589–608.
[47] National Environmental Protection Standard of the People's Republic of China. HJ 654–2013: Specifications and test procedures for ambient air quality continuous automated monitoring system for SO_2, NO_2, O_3 and CO. Chinese standard. Beijing: China Environmental Science Press; 2013. Chinese.
[48] Zhao F, Liu C, Cai Z, Liu X, Bak J, Kim J, et al. Ozone profile retrievals from TROPOMI: implication for the variation of tropospheric ozone during the outbreak of COVID-19 in China. Sci Total Environ 2021;764:142886.
[49] Rodgers CD. Inverse methods for atmospheric sounding: theory and practice. Singapore: World Scientific; 2000.
[50] Che H, Gui K, Xia X, Wang Y, Holben BN, Goloub P, et al. Large contribution of meteorological factors to inter-decadal changes in regional aerosol optical depth. Atmos Chem Phys 2019;19:10497–523.
[51] Loyola DG, Gimeno García S, Lutz R, Argyrouli A, Romahn F, Spurr RJD, et al. The operational cloud retrieval algorithms from TROPOMI on board Sentinel-5 Precursor. Atmos Meas Tech 2018;11:409–27.
[52] Sioris CE, Evans WFJ. Impact of rotational Raman scattering in the O_2A band. Geophys Res Lett 2000;27:4085–8.
[53] Bak J, Liu X, Wei JC, Pan LL, Chance K, Kim JH. Improvement of OMI ozone profile retrievals in the upper troposphere and lower stratosphere by the use of a tropopause-based ozone profile climatology. Atmos Meas Tech 2013;6:2239–54.
[54] Lamsal LN, Weber M, Tellmann S, Burrows JP. Ozone column classified climatology of ozone and temperature profiles based on ozonesonde and satellite data. J Geophys Res D Atmospheres 2004;109(D20):D20304.
[55] Zhang J, Li D, Bian J, Xuan Y, Chen H, Bai Z, et al. Long-term ozone variability in the vertical structure and integrated column over the north China Plain:

results based on ozonesonde and Dobson measurements during 2001–2019. Environ Res Lett 2021;16(7):074053.
[56] Trickl T, Vogelmann H, Ries L, Sprenger M. Very high stratospheric influence observed in the free troposphere over the northern Alps—just a local phenomenon? Atmos Chem Phys 2020;20:243–66.
[57] Ma P, Mao H, Zhang J, Yang X, Zhao S, Wang Z, et al. Satellite monitoring of stratospheric ozone intrusion exceptional events—a typical case of China in 2019. Atmos Pollut Res 2022;13(2):101297.
[58] Trickl T, Vogelmann H, Giehl H, Scheel HE, Sprenger M, Stohl A. How stratospheric are deep stratospheric intrusions? Atmos Chem Phys 2014;14:9941–61.